Versatile functionalization of de-fluorinated FMOF-1 towards enhanced carbon capture and separation: a predictive molecular simulation study†

Rashida Yasmeen, [ID] [a] Sheikh M. S. Islam, [ID] [b] Jincheng Du [ID] *[a] and Mohammad A. Omary [ID] *[b]

Fluorous metal–organic frameworks, FMOFs, represent a superhydrophobic class of MOFs containing $-CF_3$ or $-F$ groups in their pores. The primary objective of this research is to computationally design functionalized FMOF-1-X with X = $-OCH_3$, $-CN$, $-OH$, $-COOH$, and $-NH_2$ instead of $-CF_3$ and analyze their CO_2 adsorption and separation characteristics. Grand Canonical Monte Carlo (GCMC) simulations have been used to study the adsorption properties of CO_2, CH_4, and N_2 in all structures. Henry's constant (K_H) and isosteric heat of adsorption at infinite dilution (Q_{st0}) estimated from molecular Monte Carlo simulations plus the binding energy (BE) from Möller–Plesset second-order perturbation theory (MP2) quantum-mechanical simulations characterize adsorbate–adsorbent interaction strengths. Such simulations predict a systematic enhancement of all K_H, Q_{st0}, and BE values in X-functionalized MOFs *vs.* the parent FMOF-1. Among such functional MOFs, the X = $-COOH$ structure is predicted to exhibit the largest CO_2 uptake in the low-pressure region due to the strongest CO_2/$-COOH$ interaction strength, as supported by the largest K_H value (1.02×10^{-4} mol kg^{-1} Pa^{-1}). In contrast, at high pressures (30 bar), the X = $-OH$ structure is predicted to exhibit the highest CO_2 uptake. Indeed, replacing the $-CF_3$ groups in FMOF-1 by any aforementioned X group is expected to afford higher CO_2 uptake in the GCMC-simulated adsorption isotherms compared to the parent material. The selective adsorption of CO_2 over CH_4 and N_2 was determined using the ideal adsorbed solution theory (IAST) method at 50 : 50 and 15 : 85 CO_2/CH_4 and CO_2/N_2 binary mixtures, respectively. The X = $-COOH$ structure amounts to the largest selectivity (59.6 for CO_2/CH_4 and 128.7 for CO_2/N_2), *i.e.*, nearly 40× and 43× higher *vs.* FMOF-1 (1.5 and 3 for CO_2/CH_4 and CO_2/N_2, respectively) at 298 K and 0.1 bar. The study herein of functionalized MOFs for CO_2 separation, natural gas purification, landfill gas separation, and/or CO_2 flue gas capture suggest that X = $-OH$, $-COOH$, and $-NH_2$ are promising to enhance the adsorption capacity and selectivity.

1. Introduction

Traditional porous materials such as silica, activated carbons, and zeolites have been studied as potential adsorbents for carbon capture and storage (CCS) for a while.[1,2] However, these materials have not shown superior quality and bear the drawbacks of either low adsorption selectivity or smaller uptake capacity of CO_2.[3,4] In order to overcome the limitations of traditional porous solids, researchers have been exploring metal–organic frameworks (MOFs) extensively in recent times, for the enhanced adsorption and separation of CO_2.[5–8] With higher porosities and tunable chemical properties, MOFs have shown remarkable potential for adsorptive separation to date.[9–14] To achieve improved adsorption and selectivity of CO_2, the properties of MOFs could be tuned/have been tuned in different ways such as by controlling pore sizes, incorporating alkali–metal cations, introducing open metal sites, *etc.*[15–17]

Ligand functionalization[18–22] is a potential approach for the improvement of adsorbate–adsorbent interaction that could result in enhanced CO_2 adsorption in MOFs. Addition of different functional groups to a linker can significantly affect the CO_2 adsorption and separation capacities of the structures.[23,24] Arstad *et al.*[25] and An *et al.*[26] found that amine groups can improve CO_2 uptake in MOFs through the formation of larger binding sites compared to the parent MOFs.

[a]Department of Materials Science & Engineering, University of North Texas, 1155 Union Circle, Denton, Texas-76203, USA. E-mail: Jincheng.Du@unt.edu
[b]Department of Chemistry, University of North Texas, 1155 Union Circle, Denton, Texas-76203, USA. E-mail: Omary@unt.edu

Couck et al.[27] incorporated an amino group into MIL-53 (Al) and showed enhanced CO_2/CH_4 selectivity compared to the original MOF, MIL-53 (Al). Zheng et al.[28] reported higher isosteric heats of adsorption (Q_{st}) and improved CO_2 uptake in acylamide-decorated MOFs than that of the unfunctionalized structures. Improved Q_{st} was observed for amino functionalized MIL-53 (Al) as well with a value of ~38.4 kJ mol^{-1}, whereas the Q_{st} value of the parent MIL-53 (Al) was <20 kJ mol^{-1}.[27] Torrisi et al.[29,30] investigated the impact of functionalization on CO_2 adsorption by incorporating –OH, –COOH, –NH$_2$, and –CH$_3$ groups into MIL-53 (lp). As per the work, significantly higher CO_2/CH_4 selectivity was predicted for –COOH and –OH functionalized MIL-53 (lp) compared to the parent MIL-53 (lp). Gu et al.[31] used density functional theory (DFT) to study the effects of functional groups for the improvement of CO_2 uptake by introducing –SO$_3$H, –COOH, –NH$_2$, –OH, –CN, –CH$_3$, and –F groups into MOF-177. Additionally, some researchers have inspected the interaction strength of CO_2 with different functionalized linkers using ab initio methods.[32–34] Molecular simulations have been used widely by researchers to obtain useful information about the adsorption properties of MOFs, even prior to their synthesis.[35–38] Inspired by the above work, we attempted to design various functionalized FMOFs by replacing –CF$_3$ groups in the original structure by X = –OCH$_3$, –CN, –OH–, –COOH, and –NH$_2$ functional groups. Then we performed a systematic investigation of the CO_2, CH_4, and N_2 adsorption behavior of all the MOFs. Henry's constant (K_H) and isosteric heat of adsorption at infinite dilution (Q_{st0}) were obtained by Monte Carlo (MC) simulation, whereas binding energy (BE) was calculated using Möller–Plesset second-order perturbation theory (MP2). The obtained K_H, Q_{st0}, and BE values were used to understand the adsorbate–adsorbent interaction in MOFs. The CO_2 adsorption sites of MOFs were studied by analyzing the radial distribution functions (RDFs) of CO_2 at room temperature. The CO_2/CH_4 and CO_2/N_2 adsorption selectivities were determined by Grand Canonical Monte Carlo (GCMC) simulations in all the X-functionalized MOF materials. Comprehensively, we inspected the effect of the X-functional groups on the uptake capacities and selective adsorption of CO_2 over CH_4 and N_2.

2. Methodologies

2.1 Adsorbent model

FMOF-1 was considered as the reference adsorbent. This is a fluorous metal–organic framework, synthesized by Yang et al.[39] The cell parameters and the coordinates of the framework atoms were taken from the experimental crystallographic data.[40] FMOF-1 has a tetragonal crystal structure with the space group $I\bar{4}2d$ and the lattice parameters are $a = b =$ 14.0733 Å, $c = 37.675$ Å, and $\alpha = \beta = \gamma = 90°$. No experimental crystallographic data are available for FMOF-1-X (X = –OCH$_3$, –CN, –OH, –COOH, and –NH$_2$). Materials Studio was used to construct the hypothetical structures.[41] This program can efficiently generate feasible crystal structures and researchers are using this software to characterize MOF structures prior to their synthesis.[42–44] Considering FMOF-1 as the parent structure, FMOF-1-X were constructed by replacing the –CF$_3$ groups with the X-functional groups followed by structure optimization using the Forcite module, implemented in the Materials Studio program. The Universal Force Field[45] was considered to describe the interactions between the framework atoms during the structure optimization. Final structures (FMOF-1-X) were obtained after completing the two step optimization procedure. Energy and density optimization data (Fig. S1–S5; see the ESI†) ensure reliable hypothetical crystal structures. Rather than having different lattice parameters, all the FMOF-1-X exhibit the same tetragonal crystal structure as the parent FMOF-1, with the space group $I\bar{4}2d$. The optimized structures of –OCH$_3$, –CN, –OH, –COOH, and –NH$_2$ functionalized MOFs along with the parent FMOF-1 are displayed in Fig. S6–S8.† The structural properties of the MOFs such as density, void fraction and pore volume were computed using Zeo++ software,[46] whereas the RASPA2 program[47] was used to determine the accessible surface area considering N_2 as the probe molecule. The geometrical properties of all the MOFs are listed in Table 2.

2.2 Interaction potential

In order to describe the non-bonded interactions during CO_2, CH_4, and N_2 adsorption in MOFs, we used the interaction

Table 2 Geometrical properties of the MOF structures studied in this work

Structure	Density (g cm^{-3})	Pore volume (cm^3 g^{-1})	He void fraction	Surface area (m^2 g^{-1})
FMOF-1	1.666	0.248	0.413	826.537
FMOF-1-OCH$_3$	1.323	0.348	0.461	1215.416
FMOF-1-CN	1.330	0.332	0.442	1168.435
FMOF-1-OH	1.264	0.456	0.576	1492.484
FMOF-1-COOH	1.676	0.217	0.364	704.115
FMOF-1-NH$_2$	1.215	0.472	0.573	1523.289

Table 1 Binary mixture proportions and pressures for the cases studied in this work

Case	Mixture proportion	Adsorption pressure, P^{ads} (bar)	Desorption pressure, P^{des} (bar)
Natural gas purification	$CO_2/CH_4 = 10 : 90$	5	1
Landfill gas separation	$CO_2/CH_4 = 50 : 50$	1	0.1
Flue gas separation	$CO_2/N_2 = 15 : 85$	1	0.1

potential as a combination of truncated Lennard-Jones (LJ) and Coulomb potentials according to eqn (1):

$$V_{ij} = 4\varepsilon_{ij}\left[\left(\frac{\sigma_{ij}}{r_{ij}}\right)^{12} - \left(\frac{\sigma_{ij}}{r_{ij}}\right)^{6}\right] + \frac{q_i q_j}{4\pi\varepsilon_0 r_{ij}} \tag{1}$$

where the interacting atoms are indicated by i and j, r_{ij} is their interatomic distance, q_i and q_j are the partial atomic charges of i and j, respectively, ε_{ij} and σ_{ij} are the LJ potential parameters describing the well depth and repulsion distance between i and j, and ε_0 is the dielectric constant. The LJ parameters for the framework atoms were taken from the Universal Force Field (UFF)[45] as tabulated in Table S1.† The cross LJ potential parameters were calculated by invoking the Lorentz–Berthelot mixing rules. Appropriate interaction potential parameters and atomic point charges of the framework atoms are crucial for accurate molecular modeling to study the gas adsorption isotherms in MOFs. Since point charges are not obtainable experimentally, there is no particular charge calculation method that could be used widely for the estimation of the partial atomic charges of framework atoms in MOF structures.[48,49] Consequently, different methods have been developed to date to predict the partial atomic charges of the framework atoms. For instance, the work of Sladekova *et al.*[49] shows the effect of atomic point charges on the adsorption isotherms of CO_2 and H_2O in six MOFs, namely IRMOF-1, MIL-47, UiO-66, CuBTC, Co-MOF-74, and SIFSIX-2-Cu-I.

In our work, the atomic partial charges for the –CN, –OH, –COOH, and –NH$_2$ functional groups were adopted from the works of Torrisi *et al.* and Gu *et al.*[30,31] while the partial charges of –OCH$_3$ were estimated using density functional theory (DFT) implemented in the DMol3 module of Materials Studio.[41] During the DFT calculation, we used the PW91 functional along with the double-ξ numerical polarization (DNP) basis set. The partial charges of the X-functional groups were derived from the fitting of the energy surface potentials (ESPs). ESP charges are being widely used by researchers to study the gas adsorption isotherms for MOF structures,[29–31] as this method generally gives a better description of the electrostatic potential around the different atomic species in MOFs.[30] The partial charges for the rest of the framework atoms were taken from the work of Moghadam *et al.*[40] We scaled the charges a little in order to make the framework charge neutral. All the framework charges are listed in Tables S2–S7.† The long-range electrostatic interactions were calculated *via* the Ewald summation method[50] with the same cutoff distance of 12.8 Å considered for all the Lennard-Jones interactions.

In this study, CO_2 and N_2 molecules were modeled as the linear three-site rigid model,[51] whereas CH_4 was mimicked as a united spherical single site model.[52] The C–O and N–N bond lengths were 1.16 Å and 1.10 Å, respectively, in CO_2 and N_2. The charges on C and O atoms were $+0.70e$ and $-0.35e$ in CO_2. On the other hand, a charge of $-0.482e$ and $+0.964e$ was placed on N and on the center of mass, respectively, during the modeling of N_2. These partial charges on the LJ sites were used to describe the internal quadrupole moment of CO_2 and

N_2. We used the transferable potentials for the phase equilibria (TraPPE) force field to model the adsorbates (CO_2, CH_4, and N_2). The potential parameters and the atomic charges of the adsorbates are listed in Table S8.† A $2 \times 2 \times 1$ supercell was used for all MOF structures. The framework atoms were kept rigid during GCMC simulations.

2.3 Simulation details

Simulation studies have disclosed that Grand Canonical Monte Carlo (GCMC) simulations can accurately compute the gas loading in porous materials such as MOFs.[53] We used GCMC to calculate the adsorption isotherms of pure CO_2, CH_4, N_2 components, as well as binary mixtures of CO_2/CH_4 and CO_2/N_2 as a function of pressure. The calculations were carried out at 273 and 298 K up to a pressure of 30 bar in all the structures. The number of gas molecules in the adsorbed phase was allowed to fluctuate whereas the chemical potential (μ), volume (v), and temperature (T) were kept constant during the GCMC simulations. Random insertion, deletion, rotation and translation with equal probabilities were used in each MC run. The GCMC calculation at each pressure point consisted of 2.0×10^5 cycles. The first half was used for equilibration and the subsequent half was used to estimate the desired adsorption properties. Excess adsorption isotherms were simulated by considering the void fraction of both structures (details can be found in the ESI†).

Henry's constants (K_H) of the adsorbates were evaluated using the Widom particle insertion method.[54] The enthalpy of adsorption, ΔH, was determined by the statistical average of the adsorbate binding energies at different available adsorbent sites according to eqn (2):

$$\Delta H = \frac{\langle U \times N \rangle_\mu - \langle U \rangle_\mu \langle N \rangle_\mu}{\langle N^2 \rangle_\mu - \langle N \rangle_\mu^2} - \langle U_g \rangle - RT \tag{2}$$

where N is the number of adsorbed molecules, R is the universal gas constant, and $\langle \ \rangle$ defines the ensemble average.

The isosteric heat of adsorption at infinite dilution, Q_{st0}, was estimated using a single molecule of the adsorbates in the Canonical ensemble (NVT), as per the following equation:

$$Q_{st0} = -\Delta H = \langle U_{hg} \rangle - \langle U_h \rangle - \langle U_g \rangle - RT \tag{3}$$

where $\langle U_{hg} \rangle$, $\langle U_h \rangle$, and $\langle U_g \rangle$ are the average energy of the single guest molecule inside the host, the average energy of the host, and the average energy of a single guest molecule in the gas phase. The isosteric heat of adsorption at finite dilution, Q_{st}, was computed using the fluctuation method,[55] implemented in the RASPA2 software package.[47] The Q_{st} values were predicted from the fluctuations of the potential energy over the production cycles in the GCMC simulations for each pressure point.

To break down the relative contributions of van der Waals and coulombic interactions to the interaction energy between MOFs and adsorbate molecules, we performed energy minimizations of a single adsorbate molecule inside the MOF structures employing the NVT ensemble. From this force field-

based molecular simulation, the minimum host-adsorbate energy was obtained *via* Baker's method[56] and used for further analysis of the van der Waals and coulombic contributions to the interaction energy. Baker's minimization[56] for 100 independent minimization attempts with the stopping criteria of the RMS gradient of 1.0×10^{-6} was also considered to find the favorable adsorption sites of the adsorbates (CO_2, CH_4, and N_2). During Baker's minimization, framework atoms were held fixed, whereas a single molecule of the adsorbate gases was relaxed within the rigid MOF structures. Two types of trial moves, namely translation and rotation with equal probability, were attempted for the adsorbate molecules. In Baker's minimization method, the equilibrium geometries of the adsorbate molecules were estimated from the force field-based molecular simulations. All simulations, such as GCMC, Widom particle insertion calculations, and energy minimizations (*via* Baker's method), were carried out using the RASPA2 software package.[47] The binding energy (BE) of the CO_2 molecule with the various functional groups of the frameworks was computed by Möller–Plesset second-order perturbation theory (MP2) with a Def2TZVP basis set. These calculations were performed using the Gaussian 16 code.[57] Further computational details can be found in section 3.4.

We also simulated the adsorption isotherms considering the bulk composition of 50 : 50 in CO_2/CH_4 and 15 : 85 in CO_2/N_2 binary mixtures. These compositions of the binary systems represent the landfill gas separation and flue gas separation, respectively.[58] Ideal adsorbed solution theory (IAST)[59] was invoked to predict the adsorption selectivity of CO_2/CH_4 and CO_2/N_2 binary mixtures from their pure component adsorption isotherms. The selectivities were predicted at the above-mentioned composition at 298 K with a pressure range up to 0–1 bar.

All the structures were assessed in view of the three adsorbent evaluation criteria for their CO_2 separation capability over CH_4 and N_2. The adsorbent evaluation criteria are: (1) CO_2 uptake under adsorption conditions (mol kg^{-1}), N^{ads}; (2) working capacity of CO_2 (mol kg^{-1}), $\Delta N = N^{ads} - N^{des}$, and (3) selectivity, $S = \left(N^{ads}_{CO_2}/N^{ads}_W \right)(y_W/y_{CO_2})$. Here, N is the adsorbed amount, y is the gas phase mol fraction, W indicates the weakly adsorbed gas component (CH_4 or N_2), and superscripts ads and des are the adsorption and desorption conditions, respectively. We measured these parameters for three cases as listed in Table 1 and ranked all the functional FMOFs based on their selectivity.

The CO_2, CH_4, and N_2 uptake was estimated at the partial pressure of the specific gas component under the adsorption and desorption conditions.

To confirm the reliability of the force field used in this study, we first simulated N_2 adsorption in FMOF-1 at 77 K and compared it with the previously simulated data.[40] We observe a similar trend of N_2 adsorption but lower uptake compared to the previous simulated data. The slight variation in N_2 loading could be due to the different void fractions used during simulations. However, the force field is validated by the identical shape of the isotherms depicted in Fig. S9.†

3. Results and discussion

From the geometrical properties of the structures listed in Table 2, we observe increased surface areas and pore volumes of –OCH$_3$, –CN, –OH, and –NH$_2$ functionalized MOFs compared to the parent FMOF-1 structure, while we notice a decreasing trend for the density. In contrast to the other functionalized MOFs, we observe a decreased surface area and pore volume for the –COOH functionalized MOF, compared with the parent FMOF-1. Likewise, a higher density of the –COOH functionalized MOF was found. We speculate that this opposite trend for the –COOH functionalized MOF is due to the size of the bulky –COOH group compared to the other functional groups. The pore size distributions (PSDs) of the MOFs are shown in Fig. 1. The channel diameter has increased to 6.93 Å in FMOF-1-CN, 6.99 Å in FMOF-1-OH, and 6.63 Å in FMOF-1-NH$_2$ from 6.40 Å in the parent structure. On the other hand, the channel diameter has decreased to 5.55 Å and 5.31 Å, respectively, in FMOF-1-OCH$_3$ and FMOF-1-COOH.

N_2 adsorption isotherms at 77 K for all the functionalized MOFs are depicted in Fig. S10.† All the studied MOFs display type I adsorption profiles, exhibiting characteristic microporous behavior.

3.1 Energy parameters at infinite dilution

Henry's constant, K_H, and isosteric heat of adsorption at infinite dilution, Q_{st0}, can reflect the adsorbate–adsorbent interaction strength in the Henry regime. The larger K_H and Q_{st0} values indicate the greater adsorbate affinity to the adsorbent.[60] K_H and Q_{st0} values for CO_2, CH_4, and N_2 at 273 and 298 K were predicted from Monte Carlo (MC) simulations and the results at 298 K are listed in Tables 3 and 4, respectively. The values at 273 K are tabulated in Tables S9 and S10.†

The order of K_H and Q_{st0} was found as $CO_2 > CH_4 > N_2$ for all the MOFs, implying stronger CO_2–framework interactions compared to CH_4–framework and N_2–framework interactions.
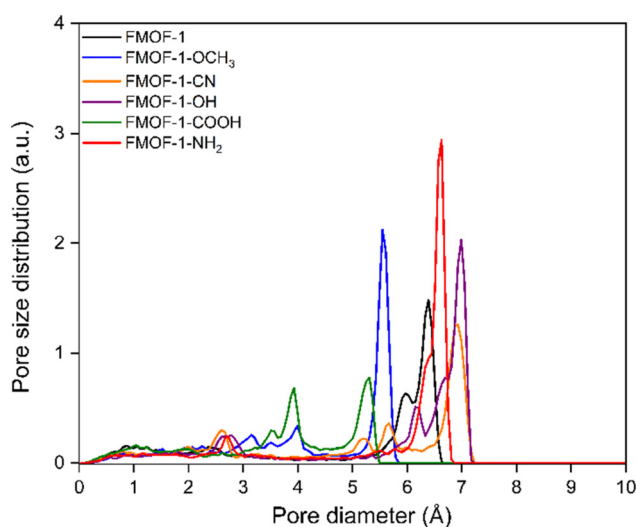

Fig. 1 Pore size distributions of the MOF structures.

Table 3 Henry's constant, K_H at 298 K

Structure	Henry constant, K_H (mol kg^{-1} Pa^{-1})		
	CO_2	CH_4	N_2
FMOF-1	1.81×10^{-6}	1.23×10^{-6}	4.95×10^{-7}
FMOF-1-OCH$_3$	4.10×10^{-6}	2.12×10^{-6}	7.55×10^{-7}
FMOF-1-CN	5.11×10^{-6}	1.34×10^{-6}	6.14×10^{-7}
FMOF-1-OH	3.64×10^{-5}	1.32×10^{-6}	7.90×10^{-7}
FMOF-1-COOH	1.02×10^{-4}	2.04×10^{-6}	9.62×10^{-7}
FMOF-1-NH$_2$	7.01×10^{-5}	2.08×10^{-6}	1.09×10^{-6}

Table 4 Isosteric heat of adsorption at infinite dilution, Q_{st0}, at 298 K

Structure	Isosteric heat of adsorption at infinite dilution, Q_{st0} (kJ mol^{-1})		
	CO_2	CH_4	N_2
FMOF-1	-13.67	-11.40	-9.01
FMOF-1-OCH$_3$	-16.94	-13.18	-10.35
FMOF-1-CN	-17.75	-11.63	-9.56
FMOF-1-OH	-29.33	-10.44	-9.63
FMOF-1-COOH	-31.04	-15.47	-14.36
FMOF-1-NH$_2$	-31.37	-11.62	-10.75

This phenomenon might be due to the larger permanent quadrupole moment of the CO_2 molecule.[61] According to the simulation, an increase in K_H and Q_{st0} (except for the Q_{st0} value of CH_4 in the –OH functionalized structure) values was noticed for all the X-functionalized MOFs compared to the parent MOF for all the adsorbates. Notably, –OH, –COOH, and –NH$_2$ groups displayed significant improvement in the K_H and Q_{st0} values for CO_2. These enhanced values of the parameters could be described by the stronger polarity of the –OH, –COOH, and –NH$_2$ groups compared to other functional groups. This assumption could be further supported by the results of the relative contribution of van der Waals (vdW) and coulombic interactions to the total interaction energy of CO_2

in the studied MOFs, which has been discussed in section 3.3. The larger K_H and Q_{st0} values of CO_2, CH_4, and N_2 in all the X-functionalized MOFs compared to the parent MOF indicate greater affinity and stronger interaction strength to the frameworks.

3.2 Pure gas adsorption isotherms

We simulated the adsorption isotherms of pure component CO_2, CH_4, and N_2 in all the X-functionalized MOFs along with the parent FMOF at 273 and 298 K with a pressure range up to 30 bar. Fig. 2 shows the CO_2 uptake for all the MOF structures at 298 K in low-pressure (0.005–1 bar) and high-pressure (1–30 bar) regions. An enhanced CO_2 uptake was observed for the X-functionalized MOFs compared to the parent MOF. The order of CO_2 uptake up to 0.2 bar (Fig. 2a) is FMOF-1-COOH > FMOF-1-NH$_2$ > FMOF-1-OH > FMOF-1-CN > FMOF-1-OCH$_3$ > FMOF-1. This is consistent with the order of the predicted Henry's constant (K_H values in Table 3). With the increase in pressure, a different CO_2 adsorption profile was observed for the studied MOFs. In the low pressure region, gas adsorption is generally dominated by the host–guest interaction,[62] as reflected in Henry's constant values. In contrast, in the high pressure region, the adsorption capacity primarily depends on the available free volume of the framework structure.[62] As shown in Fig. 2, the –COOH functionalized MOF exhibits the highest CO_2 uptake below 0.2 bar, while at 30 bar a comparable CO_2 uptake was predicted for FMOF-1-COOH and FMOF-1. This comparable CO_2 uptake is due to similar free volumes and surface areas of the structures (Table 2). At 1 bar pressure, the –OH and –NH$_2$ functionalized structures show the maximum CO_2 uptake with a value of ~3.0 mol kg^{-1}. This value is about 15-fold higher than that of the parent FMOF-1 (~0.2 mol kg^{-1}) and 1.5-fold higher than that of IRMOF-1 (2.1 mmol g^{-1} at 295 K),[63] but lower than that of zeolite NaX and NaY structures (~4.5 mol kg^{-1} at 298 K)[64,65] at 1 bar. We also observe higher CO_2 uptake for all the X-functionalized
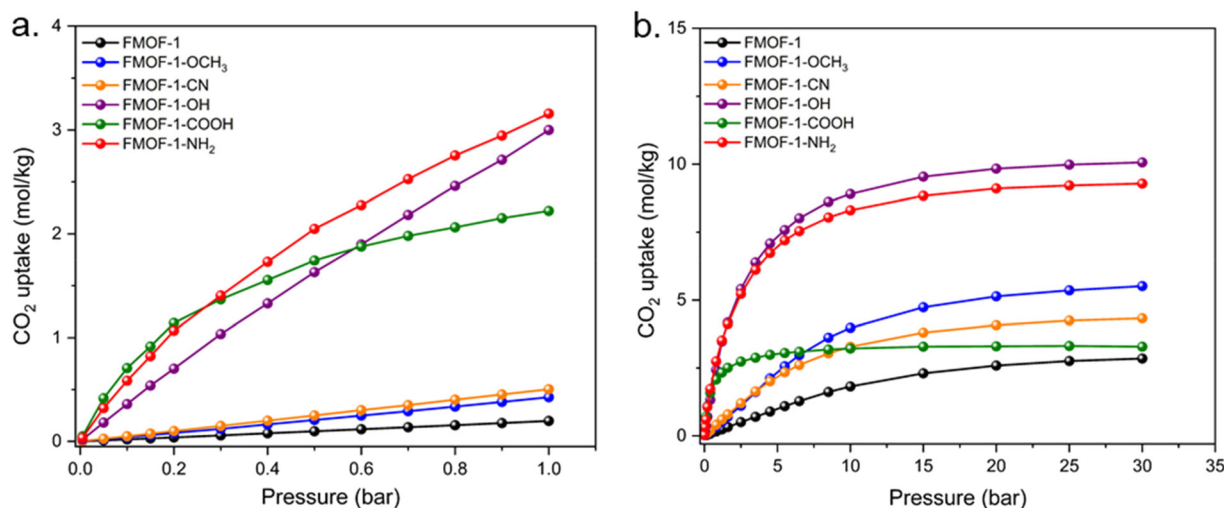
Fig. 2 CO_2 adsorption isotherms at (a) low pressure and (b) high pressure regions of MOFs at 298 K.

MOFs compared to the parent MOF in the high-pressure region. The highest CO_2 uptake was observed for FMOF-1-OH with a value of 10.07 mol kg^{-1} at 30 bar at 298 K, which is 3.35-fold higher than that of the parent FMOF-1 with a value of 2.85 mol kg^{-1}. A similar trend was observed for CO_2 adsorption isotherms at 273 K, shown in Fig. S11.†

Pure component CH_4 and N_2 adsorption isotherms at 298 K are depicted in Fig. 3 and 4 respectively, whereas Fig. S12 and S13† show the isotherms at 273 K. In the low pressure region (Fig. 3a), the order of CH_4 uptake is FMOF-1-OCH$_3$ > FMOF-1-NH$_2$ > FMOF-1-COOH > FMOF-1-CN > FMOF-1-OH > FMOF-1. For N_2 adsorption, the order was found as FMOF-1-NH$_2$ > FMOF-1-COOH > FMOF-1-OCH$_3$ > FMOF-1-OH > FMOF-1-CN > FMOF-1 (Fig. 4a). These orders of CH_4 and N_2 uptake are consistent with the orders of predicted Henry's constant (K_H values in Table 3). In the high pressure region, a different order of CH_4 and N_2 adsorption was observed for the studied MOFs.

We observe an increase in CO_2 uptake on a different scale than that of the increase in CH_4 and N_2 uptake with an increase in pressure up to 30 bar. The CO_2 adsorption isotherms exhibit a sharp rise in the low pressure region compared to CH_4 and N_2 adsorption and then reach a plateau at around 20 bar. On the other hand, CH_4 and N_2 isotherms do not show a steep uptake in the low-pressure region. This expected finding is consistent with the relatively smaller Q_{st0} values of CH_4 and N_2 compared to the Q_{st0} value of CO_2 (Table 4). CH_4 and N_2 uptake increases gradually with the pressure and does not saturate, even at the highest pressure of 30 bar. The maximum CH_4 uptake at 1 bar was observed for FMOF-1-OCH$_3$ (0.19 mol kg^{-1}) which is 1.8 times higher than that of the parent FMOF-1 (0.11 mol kg^{-1}). FMOF-1-NH$_2$ shows the maximum N_2 uptake with a value of 0.09 mol kg^{-1} which is 2.3 times higher compared to FMOF-1 (0.04 mol kg^{-1}) under the same conditions (1 bar and 298 K).
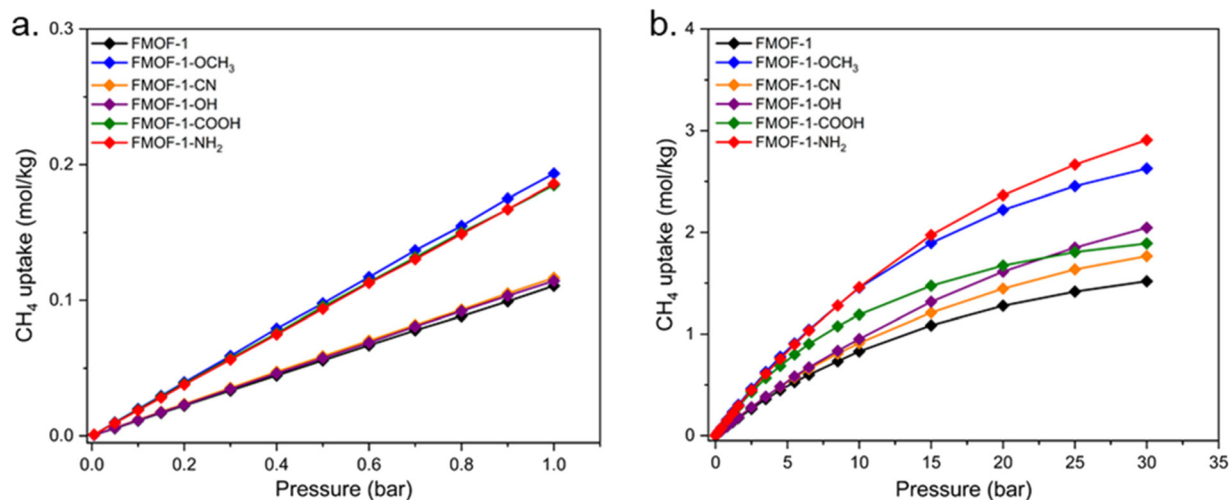

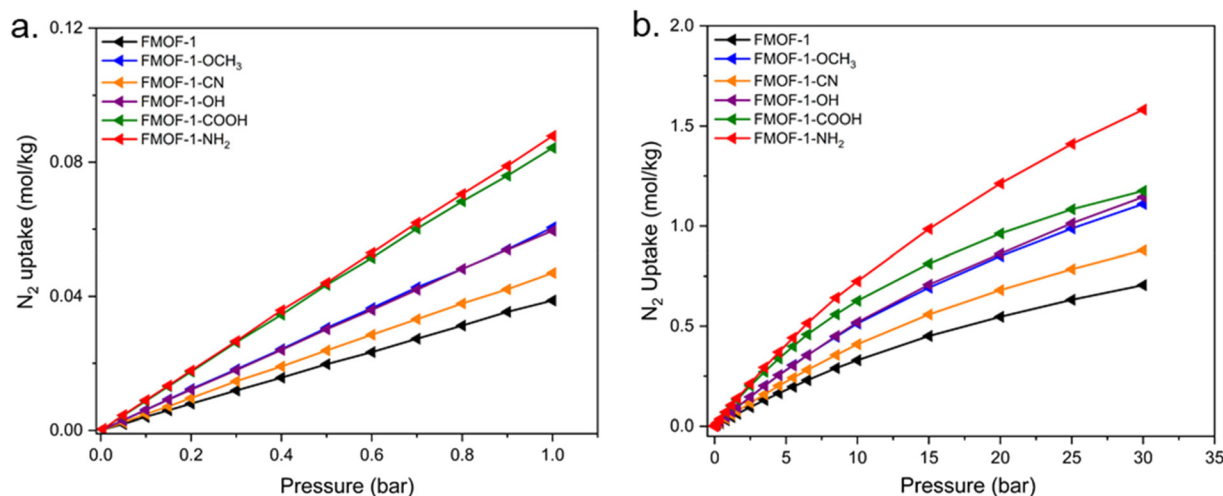Fig. 3 CH_4 adsorption isotherms at (a) low pressure and (b) high pressure regions of MOFs at 298 K.

Fig. 4 N_2 adsorption isotherms at (a) low pressure and (b) high pressure regions of MOFs at 298 K.

3.3 Isosteric heats of adsorption, Q_{st}

The isosteric heats of adsorption (Q_{st}) for CO_2, CH_4, and N_2 were obtained by GCMC simulations during the adsorption isotherm calculations. Fig. 5 and Fig. S14† display the Q_{st} values as a function of pressure and uptake, respectively, at 298 K. It is observed that, for all the MOF structures, the Q_{st} values of CO_2 are higher compared to the values obtained for CH_4 and N_2. Consequently, the order of isosteric heat of adsorption is $CO_2 > CH_4 > N_2$ for all the structures, consistent with the order of uptake capacity. At 0.005 bar, the isosteric heats of adsorption of CO_2 were estimated as 16.92, 17.70, 29.42, 30.98, and 31.07 kJ mol^{-1}, respectively, for $-OCH_3$, $-CN$, $-OH$, $-COOH$, and $-NH_2$ functionalized MOFs. All these Q_{st} values are higher compared to the Q_{st} value of CO_2 for the parent FMOF-1 (13.65 kJ mol^{-1}). The larger CO_2 Q_{st} values for the X-functionalized MOFs than that of the parent MOF over the entire pressure range demonstrates the more energetic CO_2 interaction with the X-functionalized MOFs. The CO_2 Q_{st} values of FMOF-1-OH and FMOF-1-NH_2 first decline to 29.24 and 28.15 kJ mol^{-1}, respectively, at around 5 bar (Fig. 5a) due to the adsorbate–adsorbent interaction, *i.e.*, the interactions of the CO_2 quadrupole with the most active adsorption centers of the adsorbents play the dominant role in this region. Subsequently, we notice an increasing trend of CO_2 Q_{st} with an increase in uptake or pressure, because of the increased CO_2–CO_2 interactions. For FMOF-1-COOH, the CO_2 Q_{st} first increases up to 5 bar, reaches a value of 32.23 kJ mol^{-1} and then decreases with the increase in pressure or CO_2 loadings. For FMOF-1-OH, FMOF-1-COOH, and FMOF-1-NH_2, the presence of different energetic CO_2 adsorption sites, *i.e.*, surface heterogeneity,[30] results in the maxima and minima of the Q_{st} values of CO_2 curves for these structures. For the other functionalized MOFs including the parent MOF, the relationship of Q_{st} *vs.* pressure (Fig. 5a) or Q_{st} *vs.* CO_2 uptake (Fig. S14a†) is similar. The CO_2 Q_{st} increases evenly to values of 27.69, 25.11, and 21.93 kJ mol^{-1} for FMOF-1-OCH_3, FMOF-1-CN, and FMOF-1, respectively, up to 30 bar. The increasing behavior is due to the lateral interactions of the guest molecules with the increase in pressure (or the adsorbate concentration).[66,67]

Fig. 5b and c depict the Q_{st} values of CH_4 and N_2, respectively, at 298 K. For CH_4, we observe a moderate variation in Q_{st} with an increase in pressure or CH_4 loading. The increase in CH_4 Q_{st} values was found as 11.36 to 13.47 kJ mol^{-1} for FMOF-1, 13.18 to 15.97 kJ mol^{-1} for FMOF-1-OCH_3, 11.56 to 12.96 kJ mol^{-1} for FMOF-1-CN, 10.43 to 11.90 kJ mol^{-1} for FMOF-1-OH, 15.46 to 17.42 kJ mol^{-1} for FMOF-1-COOH, and 11.58 to 13.74 kJ mol^{-1} for FMOF-1-NH_2. For FMOF-1-OH, we notice lower Q_{st} values throughout the entire pressure range compared to the parent MOF. This might be due to the larger void fraction of the –OH functionalized structure compared to the parent structure (Table 2) and the relatively smaller CH_4 K_H value (Table 3). On the other hand, FMOF-1-CN shows a decreasing trend of Q_{st} values compared to the parent MOF beyond 2.5 bar. This could be attributed to the similar K_H values of CH_4 in FMOF-1-OH and FMOF-1-CN as well as the comparable void fraction of FMOF-1-OH with FMOF-1 (0.442 *vs.* 0.413).
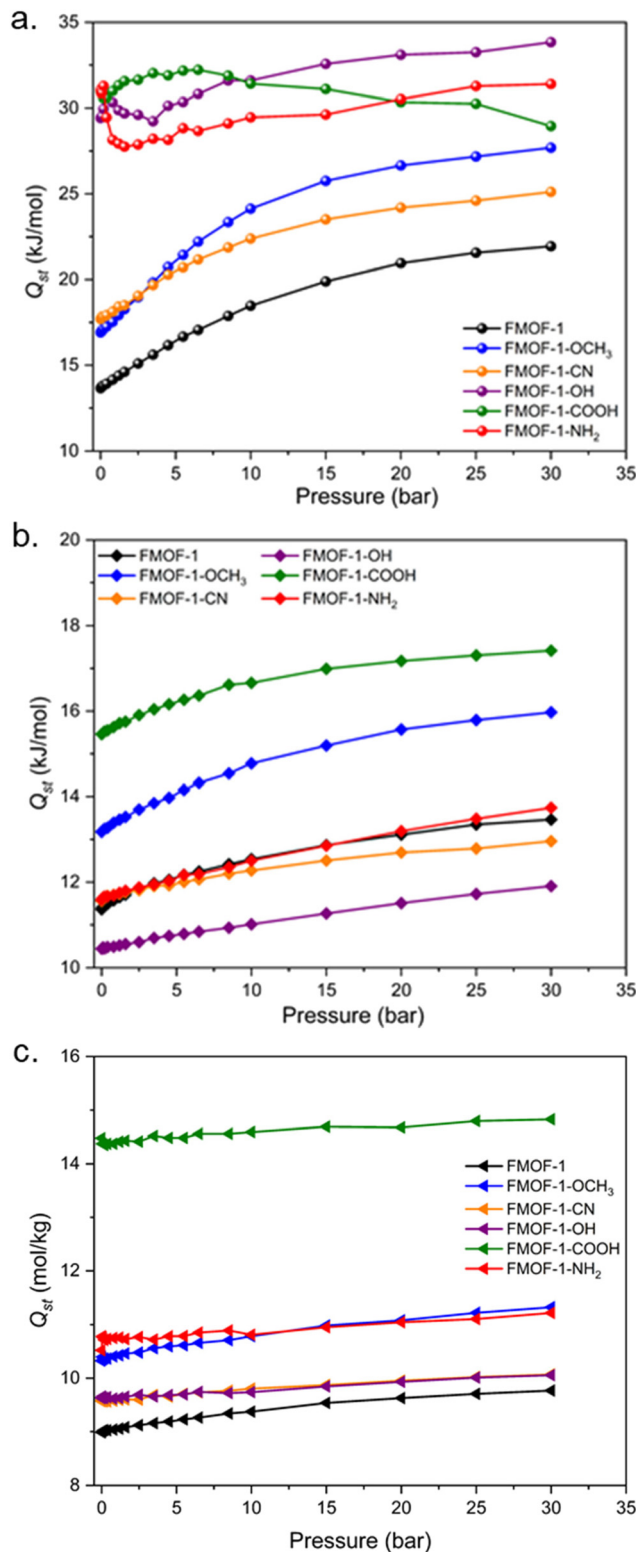

Fig. 5 GCMC simulated isosteric heats of adsorption for (a) CO_2, (b) CH_4, and (c) N_2 at 298 K up to 30 bar.

Unlike the Q_{st} values of CO_2 and CH_4, the Q_{st} value of N_2 remains almost constant throughout the entire pressure range. This outcome indicates the relatively weaker interaction of the

CH_4 and N_2 molecules with the MOF structures compared to the CO_2–MOF interactions.

It is relevant to note that enhanced CO_2, CH_4, and N_2 adsorption was observed for all the X-functionalized MOFs compared to the parent MOF, but the Q_{st} orders of CO_2, CH_4, and N_2 in those structures did not follow the same trend. This is because Q_{st} is not the only factor that reflects the adsorption isotherm, rather it is one of many factors that affect the adsorption capacity and could reflect the adsorption amount to a certain extent.[60] The Q_{st} values at 273 K are depicted in Fig. S15–S17.†

From the relative contribution of van der Waals (vdW) and coulombic interactions to the total interaction energy of CO_2, CH_4, and N_2 in the studied MOFs (Fig. 6), it is apparent that the significantly improved CO_2 adsorption capacity in –OH, –COOH, and –NH_2 functionalized structures is due to the enhanced coulombic interaction compared to the parent FMOF-1. On the other hand, for the N_2-MOF interaction energy, the vdW interactions play the dominant role with a little coulombic contribution for those structures. In contrast, the interaction energy for CH_4 was purely from the van der Waals interactions without any electrostatic contribution. This could be due to the larger quadrupole moment of CO_2 (4.30×10^{-26} esu cm^2) compared to the smaller quadrupole moment of N_2 (1.52×10^{-26} esu cm^2) and zero-quadrupole moment of CH_4.[61]

We performed additional simulations by omitting the coulombic interaction of the guest molecules with the framework atoms to investigate the effect of electrostatic interactions on CO_2, CH_4, and N_2 adsorption at 298 K up to 1 bar (Fig. 7 and S18, 19†). Disregarding the electrostatic interaction, lower CO_2 and N_2 uptake was observed for all the MOF structures. In contrast, CH_4 uptake was not influenced by turning off the coulombic interaction. We observe a larger variation of CO_2 uptake while we consider the coulombic interaction than that of the uptake without considering the coulombic interaction. For N_2 uptake, the variation was not as prominent as that of CO_2. This finding is quite consistent with the results discussed above and demonstrates the importance of electrostatic interactions on enhanced CO_2 adsorption in –OH, –COOH, and –NH_2 functionalized structures.

3.4 Interaction of CO_2 with the functional groups of the framework

The binding energy (BE) of CO_2 with various functional groups of the framework was computed using Möller–Plesset second-order perturbation theory (MP2) with a triple-ξ valence basis set with polarization (Def2TZVP).[68] The rationale for the selection of the Def2TZVP basis set is that it can efficiently capture the dispersion interaction.[6,34,69] For BE calculations between CO_2 and X-functional groups using MP2, a small model of the triazole ring containing two –CF_3 or two X-substituents (at the 3,5-positions) was constructed (Fig. 8). Only a small model was constructed to reduce the computational cost. All the models (the triazole ring containing the –CF_3 or X-substituents at the 3,5-positions) were opti-
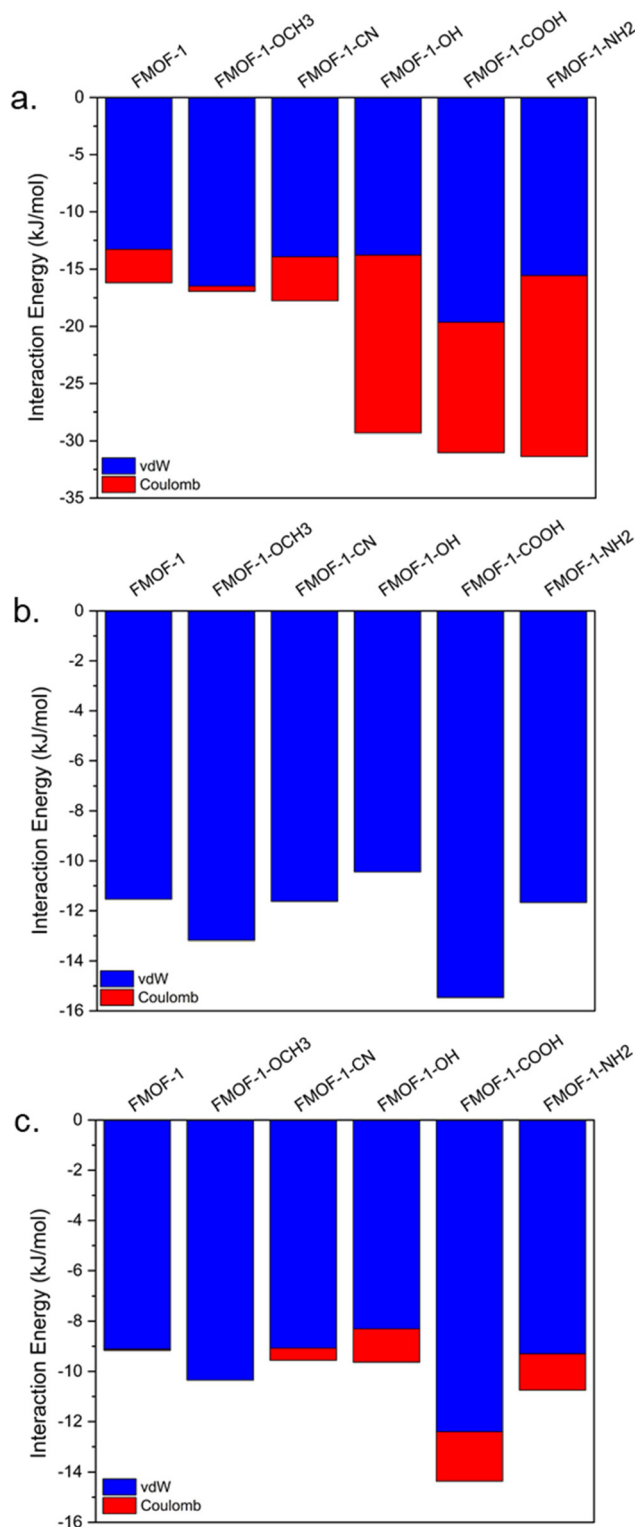

Fig. 6 Interaction energy plot for (a) CO_2, (b) CH_4, and (c) N_2 in the investigated MOFs, predicted from MC simulations.

mized first using the MP2/Def2TZVP level of theory. Then geometry optimization was done for the CO_2–triazole complex considering different geometries (positions and
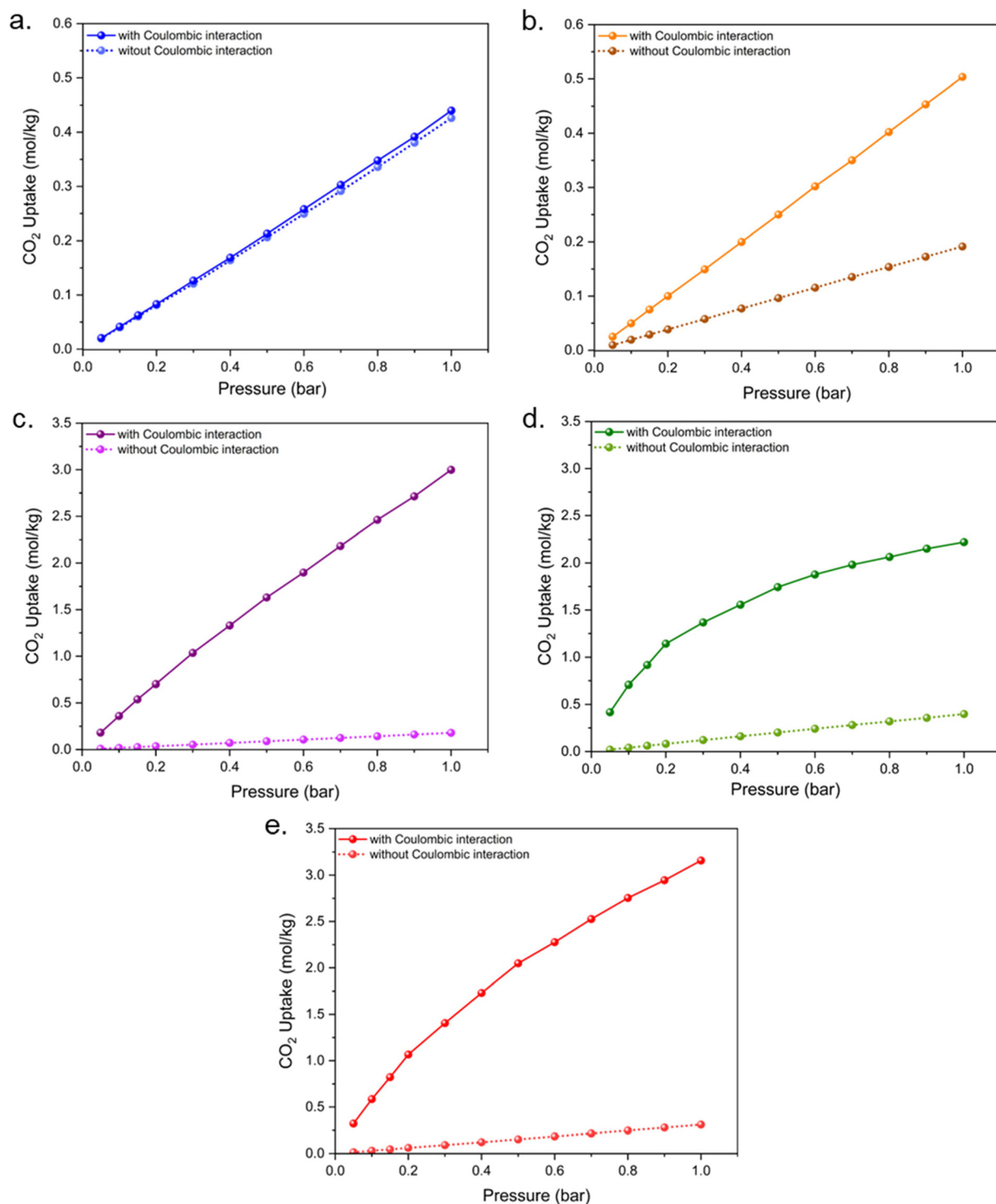
Fig. 7 Comparison of CO_2 adsorption isotherms obtained by considering or neglecting electrostatic interactions in (a) FMOF-1-OCH$_3$, (b) FMOF-1-CN, (c) FMOF-1-OH, (d) FMOF-1-COOH, and (e) FMOF-1-NH$_2$ at 298 K.

orientations) of CO_2 around the functional groups. Eventually, the BE of CO_2 around different functional groups was calculated as per the following equation:

$$\text{BE} = E_{CO_2\text{-triazole model}} - (E_{CO_2} + E_{\text{triazole model}}) \tag{4}$$

where E_{CO_2} is the energy of CO_2, $E_{\text{triazole model}}$ is the energy of the small triazole model, and $E_{CO_2\text{-triazole model}}$ is the energy of the CO_2-trizole complex in the equilibrium state. Fig. 8 shows the most stable complexes.

As per the optimized structures, the electropositive C atom of CO_2 interacts with the electronegative N and O atoms of
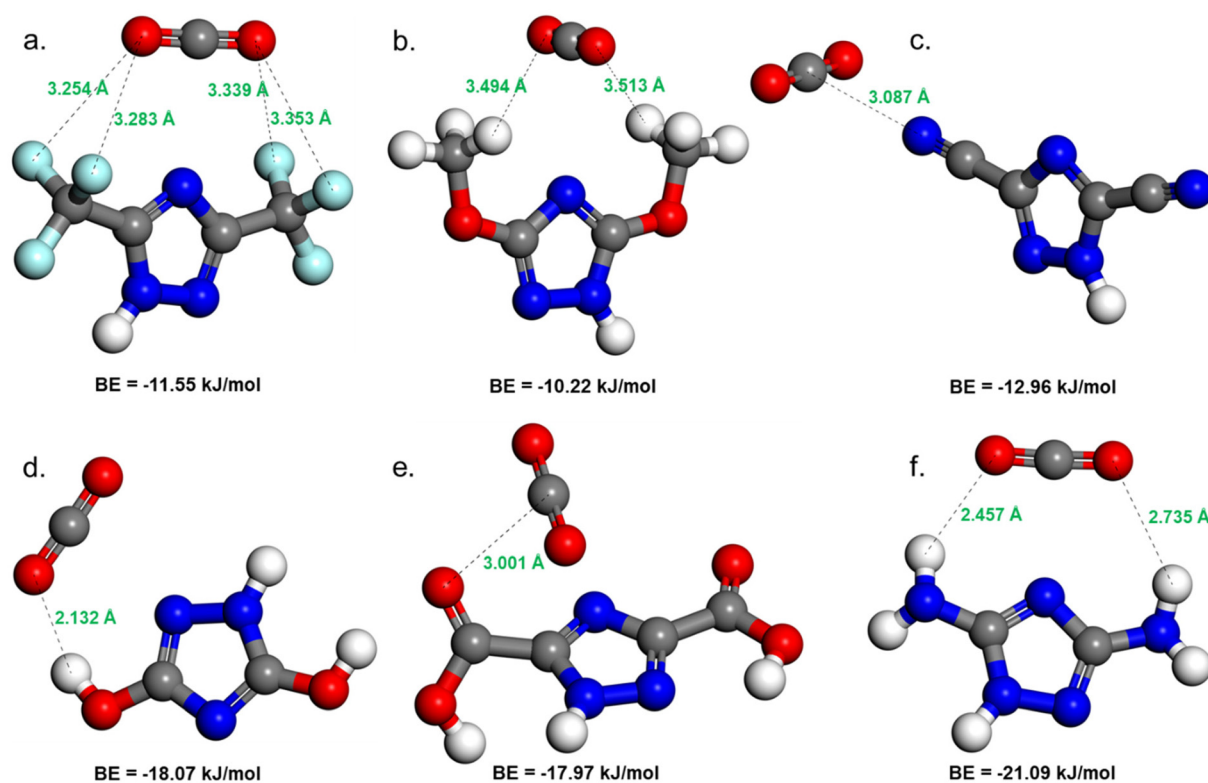
Fig. 8 Optimized structures and binding energies of CO_2 with (a) $-CF_3$, (b) $-OCH_3$, (c) $-CN$, (d) $-OH$, (e) $-COOH$, and (f) $-NH_2$ functional groups of MOFs, as per MP2 computations. Color code (C: gray, O: red, N: blue, H: white, and F: cyan).

$-CN$ and $-COOH$ functional groups, while hydrogen bonding interactions were observed for $-OCH_3$, $-NH_2$, and $-OH$ functional groups with distances of ~3.50, 2.60, and 2.13 Å, respectively. The highest binding energy value was observed for the $-NH_2-CO_2$ structure (-21.09 kJ mol^{-1}) followed by the $-OH-CO_2$ structure (-18.10 kJ mol^{-1}). Although the $O(CO_2)$ $\cdots H(-OH)$ distance exhibits a relatively smaller value (2.13 Å) than that of the average $O(CO_2)\cdots H(-NH_2)$ distance (2.60 Å), the multiple interaction between the terminal O atoms of CO_2 with the H atoms of NH_2 results in increased binding energy for the NH_2-CO_2 structure. For the $-COOH-CO_2$ structure, we notice that the CO_2 molecule is tilted towards the $O_{carbonyl}$ of the $-COOH$ group with a distance of 3.00 Å and a binding energy of -17.97 kJ mol^{-1}. We do not observe any hydrogen bonding interaction for the $-COOH-CO_2$ structure, as the $H(-COOH)$ atom is pointing away from the CO_2 molecule in the optimized configuration. The $-OCH_3-CO_2$ structure shows the least BE value (-10.22 kJ mol^{-1}) among all the structures.

The binding energies (BEs) of CO_2 with different functional groups calculated using the MP2 level of theory follow the order of FMOF-1-OCH$_3$ < FMOF-1 < FMOF-1-CN < FMOF-1-COOH < FMOF-1-OH < FMOF-1-NH$_2$ (Fig. 8). This order shows a slight disagreement from the isosteric heat of adsorption at infinite dilution, Q_{st0}, for CO_2 predicted from force field-based molecular simulation, which follows the order of FMOF-1 < FMOF-1-OCH$_3$ < FMOF-1-CN < FMOF-1-OH < FMOF-1-COOH < FMOF-1-NH$_2$ (Table 4). More precisely, we observe the dis-

agreement between FMOF-1 and FMOF-1-OCH$_3$ and between FMOF-1-COOH and FMOF-1-OH.

For the calculations obtained by MP2, we observe a large number of interactions between the CO_2 molecule and the F atoms (of $-CF_3$ groups) in FMOF-1, compared to the number of interactions between the CO_2 molecule and the H atoms (of $-CH_3$ groups) in FMOF-1-OCH$_3$. This results in an increased binding energy for the former. On the other hand, the smaller distance between $O(CO_2)\cdots H(-OH)$ (2.132 Å) compared to the distance between $C(CO_2)\cdots O_{carbonyl}$ ($-COOH$) (3.001 Å) results in a slight increase in the binding energy value for FMOF-1-OH. This disagreement for the order of Q_{st0} and BE values obtained by force field-based molecular simulation and MP2/DFT calculations has also been reported by other researchers.[6,31] However, we notice a significant enhancement of the Q_{st0} and BE values for $-COOH$, $-OH$, and $-NH_2$ functionalized structures compared to that of the parent FMOF-1 structure, using both the force field-based molecular simulation and MP2 calculations.

The radial distribution functions (RDFs), $g(r)$ between CO_2 and various functional groups of the studied MOFs at 298 K and 0.1 bar are displayed in Fig. 9. For the parent FMOF-1, the $g(r)$ value of $O(CO_2)$ around $F(-CF_3)$ is essentially zero with a distance $r < 2.50$ Å and exhibits a lower peak at ~6.38 Å. On the other hand, a pronounced peak between $O(CO_2)$ and $H(-OCH_3)$ was observed at a distance between 3.42 and 3.78 Å for FMOF-1-OCH$_3$, whereas a sharp peak between $C(CO_2)$ and
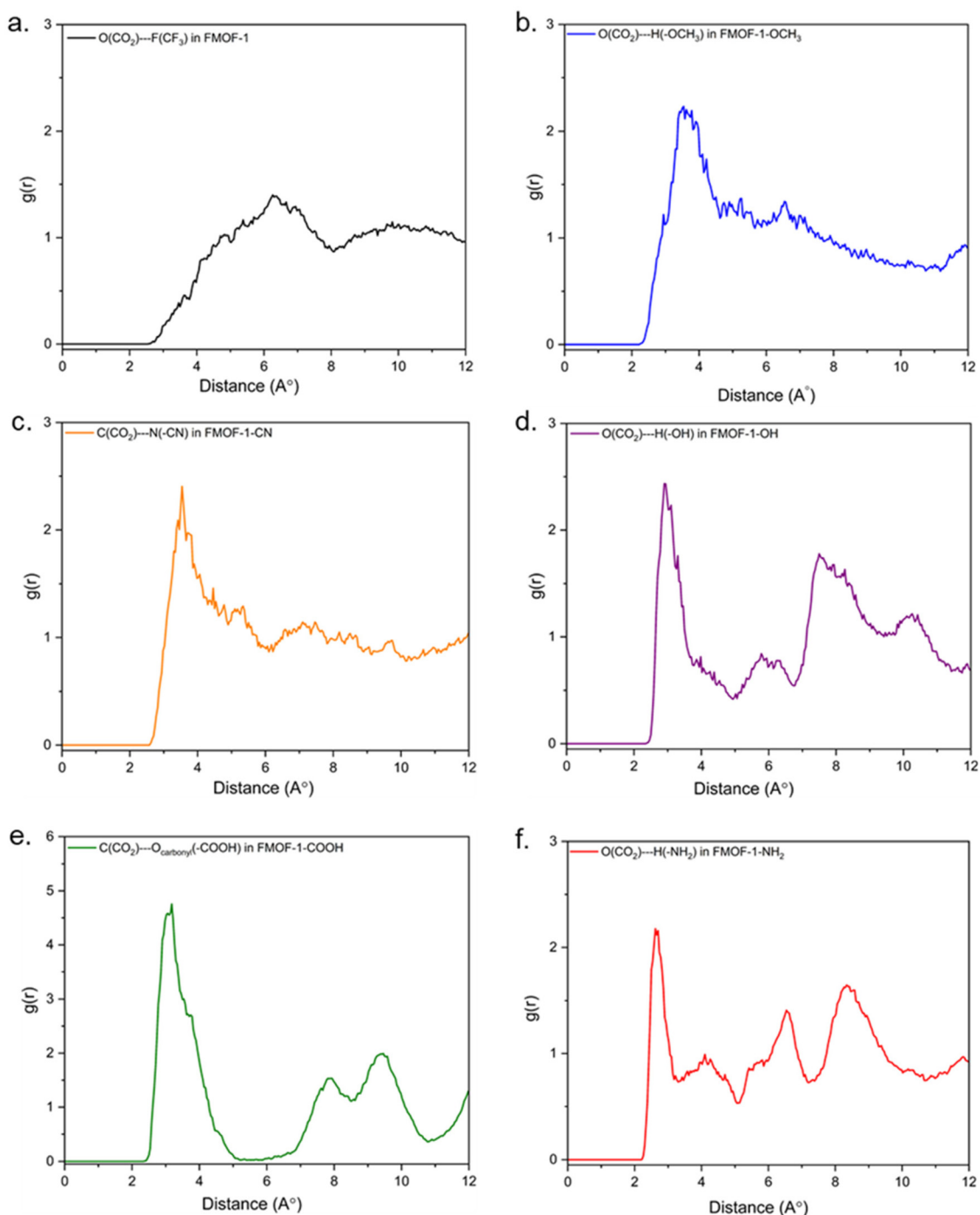
Fig. 9 Radial distribution functions for CO_2 near different functional groups of (a) FMOF-1, (b) FMOF-1-OCH$_3$, (c) FMOF-1-CN, (d) FMOF-1-OH, (e) FMOF-1-COOH, and (f) FMOF-1-NH$_2$ at 0.1 bar.

N(–CN) was found at r = 3.54 Å for FMOF-1-CN. Unlike the other MOFs, FMOF-1-OH, FMOF-1-COOH, and FMOF-1-NH$_2$ exhibit multiple peaks in $g(r)$ curves. The $g(r)$ between the O(CO$_2$) and H(–OH) for FMOF-1-OH shows two distinct peaks at 2.94 and 7.54 Å. For FMOF-1-COOH, we observe three dominant peaks between C(CO$_2$) and O$_{carbonyl}$ (–COOH) at nearly 3.00, 7.89, and 9.42 Å. Likewise, three major peaks between C(CO$_2$) and H(–NH$_2$) were found at nearly 2.66, 6.58, and

8.43 Å for FMOF-1-NH$_2$. The presence of multiple peaks in the $g(r)$ curves suggests multiple CO$_2$ interactions with neighboring ligands' X substituents in FMOF alternatives.[6] This structural analysis reveals that CO$_2$ molecules are preferentially adsorbed to X groups but at different distances, depending on the interaction strengths of CO$_2$ with the new MOF structure.

We also performed Baker's minimization by inserting a single adsorbate molecule in the X-functionalized MOFs at

298 K in order to locate the favorable adsorption sites of the adsorbates. Baker's algorithm[56] uses the eigenvalues of the Hessian matrix in order to locate true minima on the energy surface that corresponds to the equilibrium geometries. The positions of CO_2 (Fig. 10) and CH_4 & N_2 (Fig. S20†) represent the preferred binding sites of the adsorbates in MOFs, predicted by Monte Carlo (MC) simulations.

We also compared the equilibrium geometries of the adsorbate molecules after Baker's minimization, estimated from the force field-based molecular simulations with MP2 calculations. In MP2 calculations, we investigated the probable adsorption sites of CO_2 by studying their dispersion interaction energies using a small model. Only the triazole ring containing two $-CF_3$ or two X-substituents at the 3,5-positions was used in the molecular model for the study of the interaction energy of CO_2 (Fig. 8). As per the MP2 calculation, CO_2 molecules seem to interact with the $-CF_3$ group for parent FMOF-1 and X-functional groups for X-functionalized MOF structures.

On the other hand, the equilibrium geometries of CO_2 molecules after Baker's minimization estimated from the force field-based molecular simulations are shown in Fig. 10. According to Fig. 10, CO_2 molecules are preferentially adsorbed to X-functional groups rather than the metal cluster sites. This finding is fairly consistent with the adsorption sites calculated from MP2. Still, there is a slight discrepancy between the binding distances of CO_2 with X-functional groups, computed from force field-based molecular simulations and the MP2 model. For example, the distances between $O(CO_2)\cdots H(-OCH_3)$ in FMOF-1-OCH$_3$ were 3.503 and 3.601 Å, respectively, obtained from the MP2 model and force field-based molecular simulations. This little variation could be qualitatively explained by comparing the two models. In the MP2 model, we considered a small segment of the framework, where the influence of neighboring linkers on CO_2 adsorption had been ignored. In contrast, we considered the entire framework during the force field-based molecular simulations (Baker's minimization) to predict the CO_2 adsorption sites, accounting for the influence of neighboring linkers on CO_2 adsorption.

3.5 Adsorption of binary mixtures and their selectivity

We simulated the adsorption isotherms of CO_2/CH_4 and CO_2/N_2 gas mixtures with the composition of 50 : 50 and 15 : 85 molar ratios, respectively, to study the carbon capture capability from landfill and flue gases. Fig. 11 shows the adsorption isotherms of the binary mixtures for all the MOFs at 298 K up to a pressure of 1 bar. CO_2, CH_4, and N_2 adsorption exhibits a nearly linear isotherm with an increase in pressure except for CO_2 adsorption in the $-COOH$ functionalized MOF. We assume this non-linearity is due to the relatively
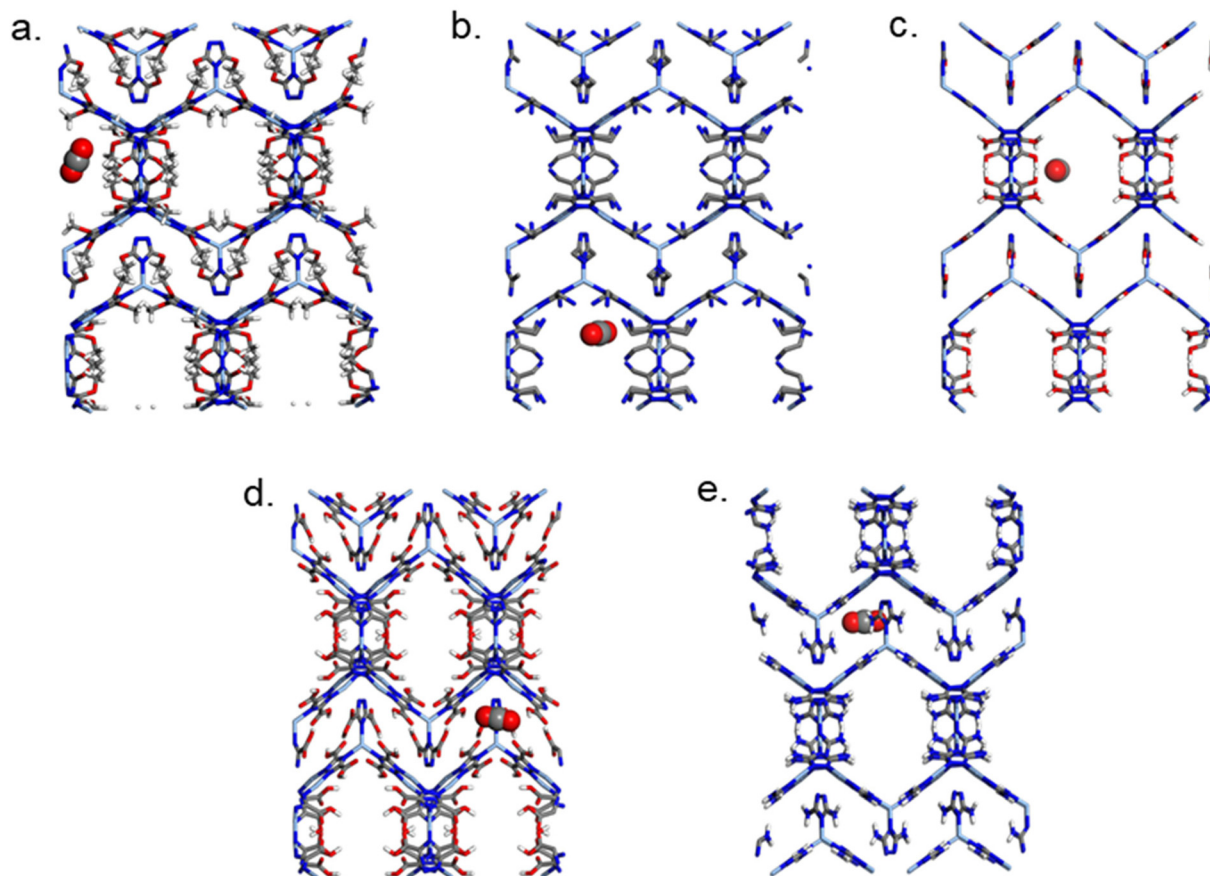

Fig. 10 Adsorption sites of CO_2 in (a) $-OCH_3$, (b) $-CN$, (c) $-OH$, (d) $-COOH$, and (e) $-NH_2$ functionalized MOFs after Baker's minimization.
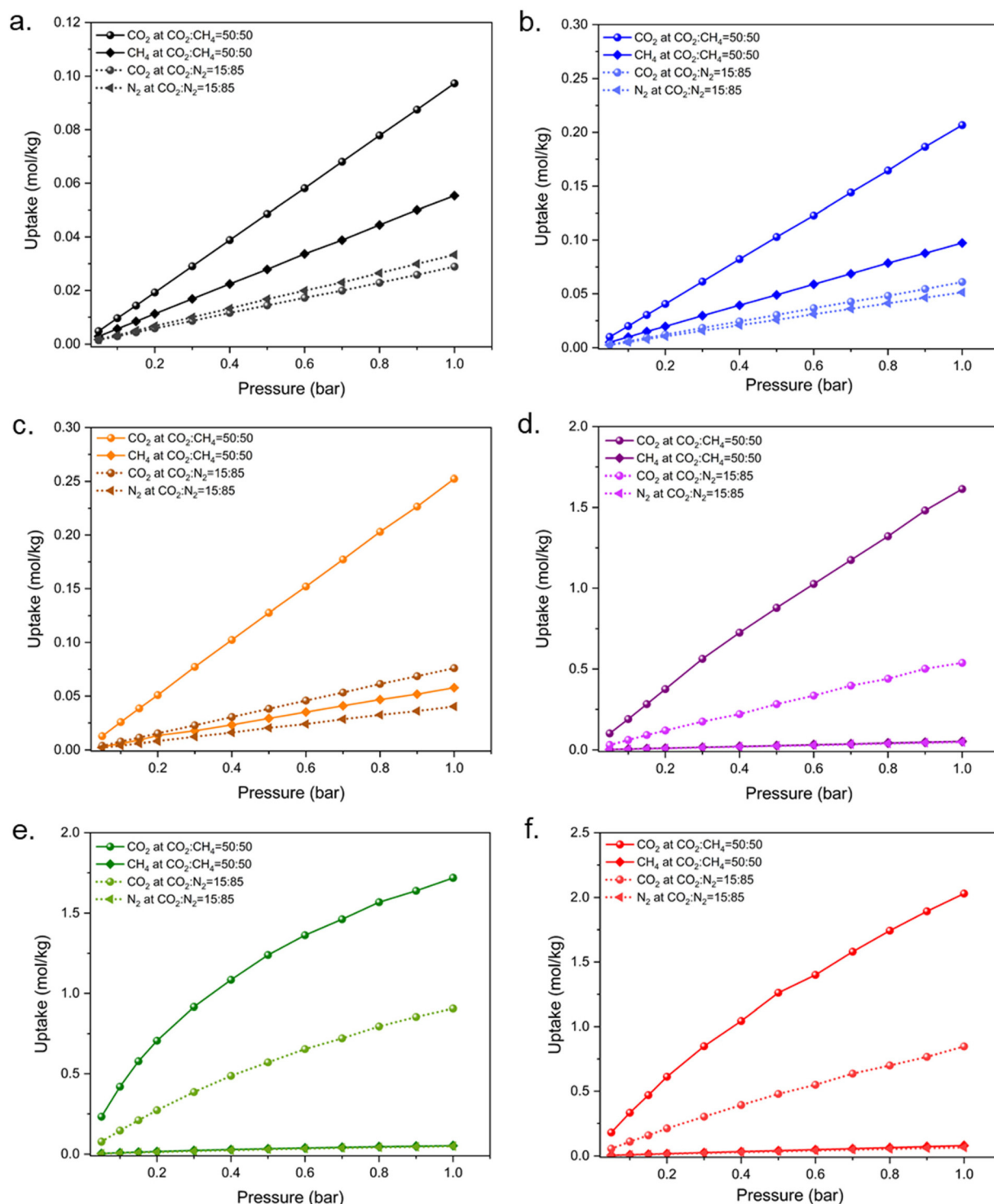
Fig. 11 Adsorption isotherms of CO_2, CH_4, and N_2 for CO_2/CH_4 (50 : 50) and CO_2/N_2 (15 : 85) binary mixtures in (a) FMOF-1, (b) FMOF-1-OCH$_3$, (c) FMOF-1-CN, (d) FMOF-1-OH, (e) FMOF-1-COOH, and (f) FMOF-1-NH$_2$ at 298 K.

higher pore volume of the other structures than that of the FMOF-1-COOH structure. We also notice preferential adsorption of CO_2 over CH_4 in all the MOFs for the CO_2/CH_4 mixture. Higher CO_2 uptake was observed for the X-functionalized

MOFs compared to the parent FMOF-1 structure. Especially for FMOF-1-NH$_2$, dominant CO_2 uptake was observed over CH_4 due to the enhanced electrostatic interaction in addition to the dispersion interactions. In the case of the CO_2/N_2 gas mixture, the

parent FMOF-1 displays higher N_2 uptake over CO_2 throughout the entire pressure range due to the higher mole fraction of N_2 in the CO_2/N_2 binary mixture. On the other hand, for the FMOF-1-OCH$_3$ and FMOF-1-CN structures, we notice lower N_2 uptake over CO_2, while for the remaining structures, vanishingly smaller N_2 uptake was observed compared to CO_2.

IAST was applied to calculate the adsorption selectivity of the MOF structures for the CO_2/CH_4 (50 : 50) and CO_2/N_2 (15 : 85) binary gas mixtures at 298 K (Fig. 12). The selectivity values exhibit a similar trend for both the mixtures. All the X-functionalized structures exhibit higher selectivity values than that of the parent MOF structure. This could be attributed to the relatively stronger CO_2 interaction with the X-functionalized MOFs.[6] It is apparent that –OH, –COOH, and –NH$_2$ functionalized MOFs significantly enhance the CO_2/CH_4 and CO_2/N_2 selectivities compared to the original FMOF-1. For the CO_2/CH_4 gas mixture, the selectivity values were obtained as 59.6, 40.0, and 31.5, respectively, for the –COOH, –NH$_2$, and –OH functionalized MOFs at a pressure of 0.1 bar. These values are much higher compared to the values obtained from –COOH, –NH$_2$, and –OH substituted MIL-53 (lp), where the selectivity values are in the range of 12–17 at 0.1 bar.[29] For the CO_2/N_2 gas mixture, FMOF-1-COOH exhibits the highest selectivity of 128.7 at 0.1 bar, which is higher than that of the dihydrofuran functional porous aromatic framework, DHF_PAF-1, having a value of 92.0 at infinite dilution.[6] For both the CO_2/CH_4 and CO_2/N_2 gas mixtures, we notice that the selectivity values remain almost constant throughout the entire pressure range for FMOF-1, FMOF-1-OCH$_3$, and FMOF-1-CN structures. On the other hand, the selectivity gradually increases with an increase in pressure for FMOF-1-OH, FMOF-1-NH$_2$, and FMOF-1-COOH structures due to the amplified CO_2–CO_2 interactions at higher pressures.[70] We also compared the selectivity values of the CO_2/CH_4 and CO_2/N_2 gas mixtures, derived from the corresponding Henry's constant ratios with the values obtained by the IAST method, at 0.1 bar and 298 K. The details of this comparison can be found in the ESI.†

3.6 Evaluation of the FMOFs for CO_2 separation

According to the adsorption evaluation criteria discussed earlier (section 2.3), we assessed the potential of all the MOFs for CO_2 separation and capture. Tables 5 and 6 rank the MOFs for natural gas purification and landfill gas separation, respectively, in terms of their selectivity values.

For natural gas purification and landfill gas separation, the MOF structures follow the order of FMOF-1-OH > FMOF-1-NH$_2$ > FMOF-1-COOH > FMOF-1-CN > FMOF-1-OCH$_3$ > FMOF-1, obtained from the selectivity calculation as observed in Tables 5 and 6. Apparently, the selectivity values for the –OH functionalized MOF are 15.50 and 16.16-fold larger than that of the parent FMOF-1 structure for natural gas purification and landfill gas separation, respectively. As shown in Table 5, FMOF-1-OH, FMOF-1-NH$_2$, and FMOF-1-COOH show relatively high

Table 5 Comparison of MOFs for natural gas purification (CO_2/CH_4 = 10 : 90)

Structure	N^{ads} (mol kg^{-1})	ΔN (mol kg^{-1})	S
FMOF-1-OH	1.63	1.26	30.06
FMOF-1-NH$_2$	2.01	1.41	23.83
FMOF-1-COOH	1.74	1.13	22.66
FMOF-1-CN	0.25	0.20	4.67
FMOF-OCH$_3$	0.21	0.17	2.40
FMOF-1	0.10	0.08	1.94

Table 6 Comparison of MOFs for landfill gas separation (CO_2/CH_4 = 50 : 50)

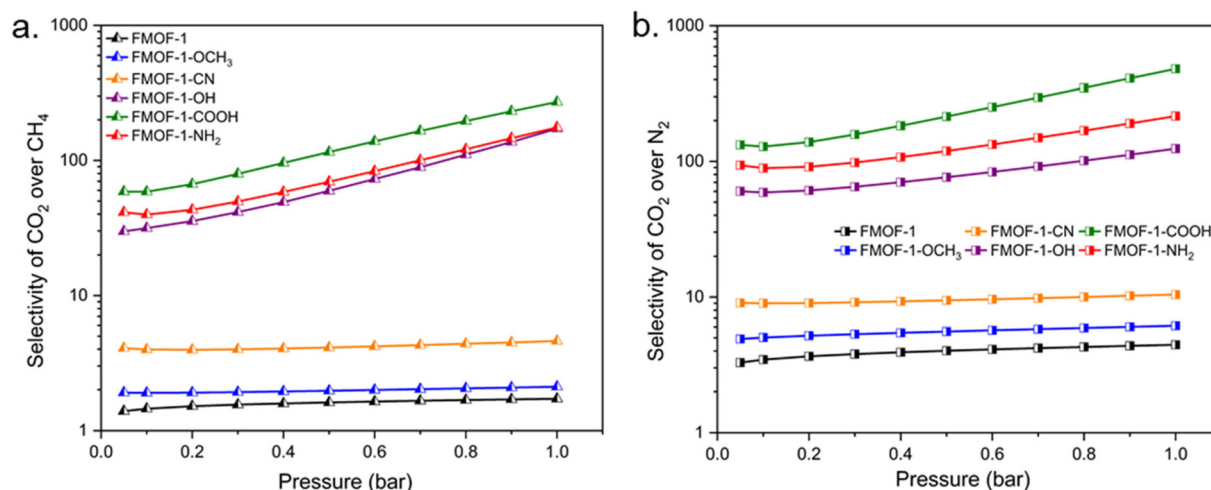| Structure	N^{ads} (mol kg^{-1})	ΔN (mol kg^{-1})	S
FMOF-1-OH	1.63	1.44	28.28
FMOF-1-NH$_2$	2.01	1.68	21.51
FMOF-1-COOH	1.74	1.33	18.42
FMOF-1-CN	0.25	0.22	4.24
FMOF-OCH$_3$	0.21	0.19	2.10
FMOF-1	0.10	0.08	1.75

Fig. 12 Adsorption selectivity for (a) CO_2/CH_4 and (b) CO_2/N_2 binary gas mixtures at 298 K, up to 1 bar, as obtained by the IAST method.

Table 7 Comparison of MOFs for flue gas separation for a $CO_2 : N_2 = 15 : 85$ binary mixture

Structure	N^{ads} (mol kg^{-1})	ΔN (mol kg^{-1})	S
FMOF-1-COOH	0.92	0.78	71.70
FMOF-1-NH$_2$	0.84	0.73	63.42
FMOF-1-OH	0.37	0.33	38.32
FMOF-1-CN	0.08	0.07	10.51
FMOF-OCH$_3$	0.06	0.05	6.68
FMOF-1	0.03	0.02	4.95

selectivity values (30.06, 23.83, and 22.66) compared to the remaining MOF structures. These values are higher than those of many materials for natural gas purification such as zeolite-5A (20.0), zeolite-13X (18.9), Mg-MOF-74 (17.3), and amine-MIL-53(Al) (16.7).[71] For landfill gas separation, the largest selectivity value was observed for the –OH functionalized MOF (28.28). This value is comparable to NaY (30.0), but smaller than that of NaX (40.0).[72] Again, the selectivity values of –OH, –NH$_2$, and –COOH functionalized MOFs (28.28, 21.51, and 18.42) are higher than those of many MOFs, for example, Mg-MOF-74 (12.5), zeolite-13X (13.2), and zeolite-5A (23.5).[71,73] The presence of highly polar –OH, –NH$_2$, and –COOH functional groups in MOFs leads to the higher adsorption of quadrupolar CO_2 than that of nonpolar CH_4 at the specified adsorption pressure, eventually resulting in larger selectivity values for the structures. Though FMOF-1-OH shows the largest selectivity value among all the structures, FMOF-1-NH$_2$ seems to be the best adsorbent with respect to N^{ads} and working capacity (ΔN) performance. We speculate these higher N^{ads} and ΔN values are due to the relatively larger pore volume of FMOF-1-NH$_2$ than those of the other structures.

For flue gas separation, the MOF structures follow a different order of performance (Table 7) compared to the above two cases, in terms of selectivity. FMOF-1-COOH shows the highest selectivity value (71.70) among all the MOFs, which is larger than those of Ni-MOF-74 (41.1) and zeolite-5A (61.8),[71] but smaller than that of NaY (500).[72] For flue gas separation, a strong CO_2–MOF interaction is desired in the low-pressure region, usually at 0.15 bar, which will lead to very high CO_2 uptake. CO_2 shows the strongest interaction with FMOF-1-COOH as indicated by the largest CO_2 K_H value (Table 3). This results in the highest CO_2 uptake for the –COOH functionalized MOF at the stated adsorption pressure, 0.15 bar (Table 7). Nevertheless, FMOF-1-COOH exhibits relatively smaller N_2 uptake (0.072 mol kg^{-1}) compared to FMOF-1-NH$_2$ (0.075 mol kg^{-1}) at 0.15 bar. Consequently, we notice the largest selectivity for FMOF-1-COOH among all the evaluated MOFs for flue gas separation.

4. Conclusions

In this work, we have systematically investigated the effect of several de-fluorinating functional groups (X = –OCH$_3$, –CN, –OH, –COOH, and –NH$_2$) on gas adsorption (CO_2, CH_4, and N_2) vs. the parent FMOF-1 (X = –CF$_3$) up to a pressure of 30

bar. Henry's constant (K_H) and isosteric heat of adsorption at infinite dilution (Q_{st0}) for CO_2 predicted via force field-based MC simulations reveal enhanced interactions between CO_2 and the X-functionalized de-fluorinated MOFs. Greater CO_2 uptake in the low-pressure region (<1 bar) is predicted for –OH, –COOH, and –NH$_2$ functionalized structures compared to the –OCH$_3$ and –CN functionalized structures. This finding suggests that the incorporation of polar functional groups into the linkers, containing lone pairs of electrons or acidic hydrogens, can significantly enhance the CO_2 adsorption capacity of MOFs. However, in the high-pressure region, the adsorption properties of the MOFs are predominantly controlled by the structural properties of the materials, such as the free volume and the surface area, rather than the nature (polar or nonpolar) of the functional groups. This was verified by comparing all the gas uptake values of the MOF structures at 30 bar. The interaction energy values between CO_2 and –COOH/–OH/–NH$_2$ functionalized structures obtained by MP2 are qualitatively similar to that of the force field-based molecular simulation values. These interaction energies along with the radial distribution function of CO_2 around different functional groups provide information about the binding sites of CO_2 in the MOF structures investigated herein. The adsorption behavior of the multicomponent mixtures was predicted from the CO_2/CH_4 and CO_2/N_2 binary systems, using GCMC simulations. FMOF-1-OH is predicted to show the highest selectivity for CO_2/CH_4, while the highest CO_2/N_2 adsorption selectivity was predicted for FMOF-1-COOH at room temperature. The adsorbent evaluation criteria data obtained for CO_2 separation indicate that –OH, –COOH, and –NH$_2$ functionalized MOFs could be a promising class of porous materials for selective CO_2 capture. These findings represent a predictive step for the experimental development of new materials towards enhancement of CO_2 separation capability, which is particularly needed for various technologies. A complementary investigation aimed at sustaining the super-hydrophobicity of FMOFs via –CH$_3$ instead of –CF$_3$ groups, hence reducing the water interference (i.e., CO_2/H_2O and CH_4/H_2O selectivity instead of CO_2/CH_4 and CO_2/N_2 selectivity herein), is described elsewhere in a sister article planned to be published back-to-back with this one.

Data availability

The data supporting this article have been included as part of the ESI.†

Conflicts of interest

The authors report no conflict of interest of any kind.

Acknowledgements

References

1 R. Krishna, *J. Phys. Chem. C*, 2009, **113**, 19756–19781.

2 R. Krishna and J. M. van Baten, *J. Membr. Sci.*, 2010, **360**, 323–333.

3 L. Kong, R. Zou, W. Bi, R. Zhong, W. Mu, J. Liu, R. P. S. Han and R. Zou, *J. Mater. Chem. A*, 2014, **2**, 17771–17778.

4 J. McEwen, J.-D. Hayman and A. Özgür Yazaydin, *Chem. Phys.*, 2013, **412**, 72–76.

5 C. Janiak and J. K. Vieth, *New J. Chem.*, 2010, **34**, 2366.

6 R. Babarao, S. Dai and D. Jiang, *Langmuir*, 2011, **27**, 3451–3460.

7 J.-R. Li, J. Sculley and H.-C. Zhou, *Chem. Rev.*, 2012, **112**, 869–932.

8 K. J. Hartlieb, J. M. Holcroft, P. Z. Moghadam, N. A. Vermeulen, M. M. Algaradah, M. S. Nassar, Y. Y. Botros, R. Q. Snurr and J. F. Stoddart, *J. Am. Chem. Soc.*, 2016, **138**, 2292–2301.

9 J. Hu, Y. Liu, J. Liu and C. Gu, *AIChE J.*, 2020, **66**, e16835.

10 Z. Zhang, Z.-Z. Yao, S. Xiang and B. Chen, *Energy Environ. Sci.*, 2014, **7**, 2868.

11 T. Düren, L. Sarkisov, O. M. Yaghi and R. Q. Snurr, *Langmuir*, 2004, **20**, 2683–2689.

12 J.-R. Li, R. J. Kuppler and H.-C. Zhou, *Chem. Soc. Rev.*, 2009, **38**, 1477.

13 R. J. Kuppler, D. J. Timmons, Q.-R. Fang, J.-R. Li, T. A. Makal, M. D. Young, D. Yuan, D. Zhao, W. Zhuang and H.-C. Zhou, *Coord. Chem. Rev.*, 2009, **253**, 3042–3066.

14 V. Finsy, S. Calero, E. García-Pérez, P. J. Merkling, G. Vedts, D. E. De Vos, G. V. Baron and J. F. M. Denayer, *Phys. Chem. Chem. Phys.*, 2009, **11**, 3515.

15 D. M. D'Alessandro, B. Smit and J. R. Long, *Angew. Chem., Int. Ed.*, 2010, **49**, 6058–6082.

16 X.-J. Wang, P.-Z. Li, Y. Chen, Q. Zhang, H. Zhang, X. X. Chan, R. Ganguly, Y. Li, J. Jiang and Y. Zhao, *Sci. Rep.*, 2013, **3**, 1149.

17 X. Liu, M. Park, S. Hong, M. Oh, J. W. Yoon, J.-S. Chang and M. S. Lah, *Inorg. Chem.*, 2009, **48**, 11507–11509.

18 S. Li, Y. G. Chung, C. M. Simon and R. Q. Snurr, *J. Phys. Chem. Lett.*, 2017, **8**, 6135–6141.

19 M. Eddaoudi, J. Kim, N. Rosi, D. Vodak, J. Wachter, M. O'Keeffe and O. M. Yaghi, *Science*, 2002, **295**, 469–472.

20 Y. H. Jhon, M. Cho, H. R. Jeon, I. Park, R. Chang, J. L. C. Rowsell and J. Kim, *J. Phys. Chem. C*, 2007, **111**, 16618–16625.

21 T. Sagara, J. Klassen, J. Ortony and E. Ganz, *J. Chem. Phys.*, 2005, **123**, 014701.

22 J. R. Karra and K. S. Walton, *J. Phys. Chem. C*, 2010, **114**, 15735–15740.

23 K. K. Tanabe and S. M. Cohen, *Chem. Soc. Rev.*, 2011, **40**, 498–519.

24 J. Hu, Y. Liu, J. Liu and C. Gu, *Fuel*, 2017, **200**, 244–251.

25 B. Arstad, H. Fjellvåg, K. O. Kongshaug, O. Swang and R. Blom, *Adsorption*, 2008, **14**, 755–762.

26 J. An, S. J. Geib and N. L. Rosi, *J. Am. Chem. Soc.*, 2010, **132**, 38–39.

27 S. Couck, J. F. M. Denayer, G. V. Baron, T. Rémy, J. Gascon and F. Kapteijn, *J. Am. Chem. Soc.*, 2009, **131**, 6326–6327.

28 B. Zheng, J. Bai, J. Duan, L. Wojtas and M. J. Zaworotko, *J. Am. Chem. Soc.*, 2011, **133**, 748–751.

29 A. Torrisi, R. G. Bell and C. Mellot-Draznieks, *Cryst. Growth Des.*, 2010, **10**, 2839–2841.

30 A. Torrisi, R. G. Bell and C. Mellot-Draznieks, *Microporous Mesoporous Mater.*, 2013, **168**, 225–238.

31 C. Gu, Y. Liu, W. Wang, J. Liu and J. Hu, *Front. Chem. Sci. Eng.*, 2021, **15**, 437–449.

32 A. Torrisi, C. Mellot-Draznieks and R. G. Bell, *J. Chem. Phys.*, 2009, **130**, 194703.

33 K. D. Vogiatzis, A. Mavrandonakis, W. Klopper and G. E. Froudakis, *ChemPhysChem*, 2009, **10**, 374–383.

34 A. Torrisi, C. Mellot-Draznieks and R. G. Bell, *J. Chem. Phys.*, 2010, **132**, 044705.

35 T. Düren, Y.-S. Bae and R. Q. Snurr, *Chem. Soc. Rev.*, 2009, **38**, 1237.

36 D. H. Jung, D. Kim, T. B. Lee, S. B. Choi, J. H. Yoon, J. Kim, K. Choi and S.-H. Choi, *J. Phys. Chem. B*, 2006, **110**, 22987–22990.

37 A. Martín-Calvo, E. García-Pérez, J. M. Castillo and S. Calero, *Phys. Chem. Chem. Phys.*, 2008, **10**, 7085.

38 T. Sagara, J. Klassen and E. Ganz, *J. Chem. Phys.*, 2004, **121**, 12543–12547.

39 C. Yang, X. Wang and M. A. Omary, *J. Am. Chem. Soc.*, 2007, **129**, 15454–15455.

40 P. Z. Moghadam, J. F. Ivy, R. K. Arvapally, A. M. dos Santos, J. C. Pearson, L. Zhang, E. Tylianakis, P. Ghosh, I. W. H. Oswald, U. Kaipa, X. Wang, A. K. Wilson, R. Q. Snurr and M. A. Omary, *Chem. Sci.*, 2017, **8**, 3989–4000.

41 *Material Studio Modeling Environment, Release 6*, Accelrys Software Inc., San Diego, California, USA, 2011.

42 D. A. Gomez-Gualdron, O. V. Gutov, V. Krungleviciute, B. Borah, J. E. Mondloch, J. T. Hupp, T. Yildirim,

O. K. Farha and R. Q. Snurr, *Chem. Mater.*, 2014, **26**, 5632–5639.

43 O. K. Farha, A. Özgür Yazaydın, I. Eryazici, C. D. Malliakas, B. G. Hauser, M. G. Kanatzidis, S. T. Nguyen, R. Q. Snurr and J. T. Hupp, *Nat. Chem.*, 2010, **2**, 944–948.

44 O. V. Gutov, W. Bury, D. A. Gomez-Gualdron, V. Krungleviciute, D. Fairen-Jimenez, J. E. Mondloch, A. A. Sarjeant, S. S. Al-Juaid, R. Q. Snurr, J. T. Hupp, T. Yildirim and O. K. Farha, *Chem. – Eur. J.*, 2014, **20**, 12389–12393.

45 A. K. Rappe, C. J. Casewit, K. S. Colwell, W. A. Goddard and W. M. Skiff, *J. Am. Chem. Soc.*, 1992, **114**, 10024–10035.

46 T. F. Willems, C. H. Rycroft, M. Kazi, J. C. Meza and M. Haranczyk, *Microporous Mesoporous Mater.*, 2012, **149**, 134–141.

47 D. Dubbeldam, S. Calero, D. E. Ellis and R. Q. Snurr, *Mol. Simul.*, 2016, **42**, 81–101.

48 M. Sedighi, M. R. Talaie, H. Sabzyan, S. Aghamiri and P. Chen, *Fuel*, 2022, **308**, 121965.

49 K. Sladekova, C. Campbell, C. Grant, A. J. Fletcher, J. R. B. Gomes and M. Jorge, *Adsorption*, 2020, **26**, 663–685.

50 P. P. Ewald, *Ann. Phys.*, 1921, **369**, 253–287.

51 J. J. Potoff and J. I. Siepmann, *AIChE J.*, 2001, **47**, 1676–1682.

52 M. G. Martin and J. I. Siepmann, *J. Phys. Chem. B*, 1998, **102**, 2569–2577.

53 D. Frenkel and B. Smit, *Understanding Molecular Simulation: From algorithm to Applications*, Elsevier Inc., 2023.

54 B. Widom, *J. Chem. Phys.*, 1963, **39**, 2808–2812.

55 T. J. H. Vlugt, E. García-Pérez, D. Dubbeldam, S. Ban and S. Calero, *J. Chem. Theory Comput.*, 2008, **4**, 1107–1118.

56 J. Baker, *J. Comput. Chem.*, 1986, **7**, 385–395.

57 M. J. Frisch, G. W. Trucks, H. B. Schlegel, G. E. Scuseria, M. A. Robb, J. R. Cheeseman, G. Scalmani, V. Barone, G. A. Petersson, H. Nakatsuji, X. Li, M. Caricato, A. V. Marenich, J. Bloino, B. G. Janesko, R. Gomperts, B. Mennucci, H. P. Hratchian, J. V. Ortiz, A. F. Izmaylov, J. L. Sonnenberg, D. Williams-Young, F. Ding, F. Lipparini, F. Egidi, J. Goings, B. Peng, A. Petrone, T. Henderson, D. Ranasinghe, V. G. Zakrzewski, J. Gao, N. Rega, G. Zheng, W. Liang, M. Hada, M. Ehara, K. Toyota, R. Fukuda, J. Hasegawa, M. Ishida, T. Nakajima, Y. Honda, O. Kitao, H. Nakai, T. Vreven, K. Throssell, J. A. Montgomery Jr., J. E. Peralta, F. Ogliaro, M. J. Bearpark, J. J. Heyd, E. N. Brothers, K. N. Kudin, V. N. Staroverov, T. A. Keith, R. Kobayashi, J. Normand, K. Raghavachari, A. P. Rendell, J. C. Burant, S. S. Iyengar, J. Tomasi, M. Cossi, J. M. Millam, M. Klene, C. Adamo, R. Cammi, J. W. Ochterski, R. L. Martin, K. Morokuma, O. Farkas, J. B. Foresman and D. J. Fox, *Gaussian 16, Revision C.01*, Gaussian, Inc., Wallingford CT, 2016.

58 C. Altintas, G. Avci, H. Daglar, A. Nemati Vesali Azar, S. Velioglu, I. Erucar and S. Keskin, *ACS Appl. Mater. Interfaces*, 2018, **10**, 17257–17268.

59 A. L. Myers and J. M. Prausnitz, *AIChE J.*, 1965, **11**, 121–127.

60 L. Qu, Z. Wang and L. Liu, *Fire*, 2023, **6**, 355.

61 P. Chowdhury, S. Mekala, F. Dreisbach and S. Gumma, *Microporous Mesoporous Mater.*, 2012, **152**, 246–252.

62 Z. Cai, C. E. Bien, Q. Liu and C. R. Wade, *Chem. Mater.*, 2020, **32**, 4257–4264.

63 S. R. Caskey, A. G. Wong-Foy and A. J. Matzger, *J. Am. Chem. Soc.*, 2008, **130**, 10870–10871.

64 S. Cavenati, C. A. Grande and A. E. Rodrigues, *J. Chem. Eng. Data*, 2004, **49**, 1095–1101.

65 K. S. Walton, M. B. Abney and M. D. LeVan, *Microporous Mesoporous Mater.*, 2006, **91**, 78–84.

66 S. M. S. Islam, R. Yasmeen, G. Verma, S. M. Tekarli, V. N. Nesterov, S. Ma and M. A. Omary, *Inorg. Chem.*, 2024, **63**, 8664–8673.

67 H. W. B. Teo, A. Chakraborty and S. Kayal, *Appl. Therm. Eng.*, 2017, **110**, 891–900.

68 R. Ahlrichs, M. Bär, M. Häser, H. Horn and C. Kölmel, *Chem. Phys. Lett.*, 1989, **162**, 165–169.

69 Z. Xiang, S. Leng and D. Cao, *J. Phys. Chem. C*, 2012, **116**, 10573–10579.

70 Y. Chen and J. Jiang, *ChemSusChem*, 2010, **3**, 982–988.

71 Y. Bae and R. Q. Snurr, *Angew. Chem., Int. Ed.*, 2011, **50**, 11586–11596.

72 R. Krishna and J. M. van Baten, *Phys. Chem. Chem. Phys.*, 2011, **13**, 10593.

73 D. Saha, Z. Bao, F. Jia and S. Deng, *Environ. Sci. Technol.*, 2010, **44**, 1820–1826.